Check for updates

Impact of Locally Administered Carboxydextran-Coated Super-Paramagnetic Iron Nanoparticles on Cellular Immune Function

*Luisa Pedro, Quentin Harmer, Eric Mayes, and Jacqueline D. Shields**

Interstitially administered iron oxide particles are currently used for interoperative localization of sentinel lymph nodes (LNs) in cancer staging. Several studies have described concerns regarding the cellular accumulation of iron oxide nanoparticles relating them to phenotype and function deregulation of macrophages, impairing their ability to mount an appropriate immune response once an insult is present. This study aims to address what phenotypic and functional changes occur during lymphatic transit and accumulation of these particles. Data show that 60 nm carboxydextran-coated iron nanoparticles use a noncellular mechanism to reach the draining LNs and that their accumulation in macrophages induces transient phenotypic and functional changes. Nevertheless, macrophages recover their baseline levels of response within 7 days, and are still able to mount an appropriate response to bacterially induced inflammation.

1. Introduction

The use of super-paramagnetic iron oxide (SPIO) nanoparticles in biomedical applications has been the subject of extensive and growing research in the past ten years. SPIO nanoparticles are attractive for clinical use because they can form stable biocompatible, colloidal suspensions when coated, they are only magnetic in the presence of an applied field, they can be conjugated with a range of ligands and molecules, and they can be broken down by the body. This combination of features has resulted in proposed applications including imaging, sensing, targeted drug delivery, therapeutic heating (hyperthermia), and mechanical stimulation.[1,2]

Dr. L. Pedro, Dr. J. D. Shields
MRC Cancer Unit
University of Cambridge
Hutchison/MRC Research Centre
Box 197, Cambridge Biomedical Campus, Cambridge CB2 0XZ, UK
E-mail: js970@mrc-cu.cam.ac.uk
Dr. Q. Harmer, Dr. E. Mayes
Endomagnetics Ltd.
The Jeffreys Building
St John's Innovation Park, Cowley Road, Cambridge CB4 0WS, UK

The ORCID identification number(s) for the author(s) of this article can be found under https://doi.org/10.1002/smll.201900224.

Much of this research is yet to be translated out of the laboratory, and iron oxide nanoparticle products approved for clinical use are more limited.[3–6] SPIO nanoparticles were first approved for use as intravenous magnetic resonance imaging (MRI) contrast agents due to their strong T1 and T2 relaxivities,[7] and later as an iron replacement therapy. More recently, iron oxide nanoparticle suspensions have been approved for lymph node (LN) mapping and detection as part of cancer staging.[8] In this application, a colloidal suspension of SPIO particles is injected locally into interstitial tissue near the tumor. The particles are sized such that they are taken up by the lymphatics[9] and migrate to the draining "sentinel" LNs where they accumulate. The magnetized nodes can be detected and localized during surgery using a handheld magnetic probe.[10,11] This sentinel node biopsy procedure is an important part of staging a number of cancers, particularly breast cancer and malignant melanoma, and the magnetic technique has been proved to be a safe and effective alternative to the previous standard technique that uses a radio-labeled tracer to detect the sentinel nodes.[11–14]

The fate of intravenously administered SPIO nanoparticles for MRI and iron replacement is well understood: they are rapidly taken up by Kupffer cells in the liver and other cells of the mononuclear phagocyte system, after which they are metabolized and regulated by normal physiological iron homeostatic mechanisms.[15] However, the mechanism of uptake and the fate of locally delivered SPIO nanoparticles are less well described. In breast cancer patients, it has been shown that locally delivered SPIO rapidly accumulates in sinuses and the subcapsular space of sentinel lymph nodes (SLNs),[13] but the mechanisms by which SPIO was transported to the draining LNs and longer-term effects have not been investigated.

The size and properties of particles can determine the rate at which they transit by mechanical means to LNs,[16–23] ranging from seconds to a day,[17,24,25] with optimal transport via lymphatics achieved in particles between 20 and 60 nm in diameter. By contrast, cellular transport via loaded antigen-presenting cells takes from 2 to 24 h to traffic from the peripheral tissue to the LN,[25–31] and subsequent retention of particulates in the LNs depends on size[32–34] and retention by phagocytic cells.[35,36]

Initial analysis of injected nanoparticles in in vivo models and cancer patients indicated that, longer-term, accumulation in tissue macrophages was possible following scavenging at the injection site or respective draining LN. This raises the potential concern that accumulation of iron oxide nanoparticles may

**ADVANCED
SCIENCE NEWS**
www.advancedsciencenews.com

small
NANO · MICRO
www.small-journal.com

induce phenotype and functional deregulation of macrophages impairing their ability to mount an appropriate immune response once an insult is present.

A growing number of studies have investigated cellular changes brought about by uptake of engineered SPIO nanoparticles, however, results varied dramatically between cell types. Also, particles examined had different sizes (which can differ between 20 and 150 nm) and different surface coatings[37] (which influence particle biodistribution and cellular uptake), therefore inducing different cellular responses. In nonimmune neuronal cells, uptake of dextran-coated SPIO nanoparticles induced changes in the expression of a large number of genes, including genes related to iron homeostasis,[38] albeit transiently. By contrast, these SPIO nanoparticles had no impact on leukocyte proliferation but induced slight immune-suppressor effects (such as inducing expression of interleukin (IL)-10 and members of the tumor necrosis factor (TNF) family of proteins), as well as reducing monocyte cell migration.[37,39] In macrophages, carbohydrate-coated SPIO nanoparticles induced proinflammatory (M1) responses, leading to inhibition of tumor growth in mammary and lung cancer metastasis in the liver and lungs.[40] Whereas SPIO nanoparticles coated with dimercapto-succinic acid, 3-aminopropyl-triethoxysilane, or aminodextran exhibited no effect in proliferation but induced changes in iron metabolism, increases in reactive oxygen species (ROS), and induction of anti-inflammatory (M2) phenotypes with reduced macrophage random migration and concurrent increased chemotaxis.[41] The latter was also a feature for citrate and malate-coated SPIO nanoparticles.[42] Carboxydextran-coated SPIO nanoparticles induced increases in endosomal recycling in human mesenchymal stem cells[43] and pushed M2 macrophages toward a M1-like phenotype.[44] Deregulation of macrophage activation from an M1 to a M2-like activation state upon LPS (bacterial lipopolysaccharide) inflammatory stimulus was also described, characterized by suppression of IL-10 production, enhanced TNF-alpha production, and diminished phagocytic ability.[37] However, the majority of these studies focus on immediate, short-term effects after exposure to SPIO nanoparticles and do not address longer-term effects of SPIOs. Thus, we sought to address the kinetics and means carboxydextran-coated SPIO nanoparticles use to reach the draining LN, and potential long-term implications of its accumulation, both in the injection site and the downstream LN. Here, we show that carboxydextran-coated SPIO nanoparticles rapidly transit to draining LNs via mechanical transport rather than via cell-dependent means. While particles persist at injection sites and LNs where they may be sampled by macrophages, no long-term impact on macrophage phenotype or functional capacity were observed in vitro or in vivo.

2. Results and Discussion

2.1. Mechanisms of SPIO Nanoparticle Transport to Lymph Nodes

To determine the means by which carboxydextran-coated SPIO nanoparticles reach the LN, i.e., mechanical versus cellular transport, a time course assay was performed in which a SPIO nanoparticle suspension was administered in conjunction with tetramethylrhodamine-5-(and 6)-isothiocyanate (TRITC) paint.

TRITC painting gives a measure of cell migration from peripheral tissues to LNs, where peripheral antigen presenting cells are stimulated by the sensitizing agents or "danger signal" within the TRITC paint, which they engulf, and carry to the LNs. On a gross scale, it was immediately apparent that SPIO nanoparticles had reached LNs at the earliest time points examined (10 min post administration). In contrast to non draining nodes, which were pearlescent white, a brown signal was observed in the capsular regions of draining nodes (**Figure 1**a). Confocal analyses confirmed that SPIO rapidly reached draining LNs and could be detected by its carboxydextran coating within 10 min of inoculation (Figure 1b), but no TRITC positive cells were present. At 10 min, SPIO were found predominantly in the subcapsular sinus, colocalized with lymphatic structures (marked by the lymphatic-specific glycoprotein LYVE-1) and to a lesser extent, deeper lymphatic structures of the medullary sinuses (Figure 1b). While SPIO was predominantly localized to LYVE-1+ lymphatics, some association with CD11b/F480/sialoadhesin-expressing macrophages that line the sub-capsular sinus in close proximity to vessels was observed (Figure S1a, left panel, Supporting Information). By 24 h, SPIO was still observed in the subcapsular sinus but was also detected associated with deeper medullary lymphatics (Figure S1b, Supporting Information). In contrast to early time points, by 24 h, abundant TRITC positive cells were detected in the cortex of LNs (Figure 1b, right panel). The kinetics observed were consistent with SPIO possessing the optimal physical properties required for lymphatic-specific uptake and subsequent transport via lymph flow to LN.[16–23]

Further characterization of LNs by flow cytometry demonstrated that levels of cell-associated SPIO remained at consistent low levels throughout all time points tested (Figure 1c). Such low detection levels indicated that the majority of SPIO identified in LNs was indeed "free" within circulating lymph rather than cellular. By contrast, TRITC positive cells, i.e., those that engulfed matter in the peripheral dermis and then migrated, were only detected at the 24 h time point (Figure 1d,e). The discrepancy in LN homing kinetics between SPIO versus cell transport (10 min vs 24 h, respectively) together with the lack of colocalization of dextran and TRITC-labeled cells supported a mechanical mechanism governed by normal lymphatic drainage function over cell-mediated methods as the primary mode of particle transport for the SPIOs. From initial flow cytometry analysis, it remained unclear as to whether the small amounts of cellular SPIO detected on CD45+ cells were "associated" with the cell surface or had in fact been internalized. To address this, staining cell surface-associated SPIO was followed by a permeabilization step before a second antibody incubation. This would allow detection of total cellular SPIO. Flow cytometric analysis confirmed no significant increases in SPIO immune cells upon permeabilization (Figure 1c), consistent with the notion that SPIO was not bound and internalized for degradation or antigenic sampling. While we did observe some localization of SPIO with macrophages, more so at later time points, we depleted macrophages using liposomal clodronate (clodrosome) prior to SPIO injections to determine if macrophages contributed to SPIO transport and localization (Figure 1a), but no change in the drainage or accumulation kinetics was observed.

To address the possibility of delayed arrival of TRITC-labeled cell to LNs as a consequence of the requirement for TRITC and
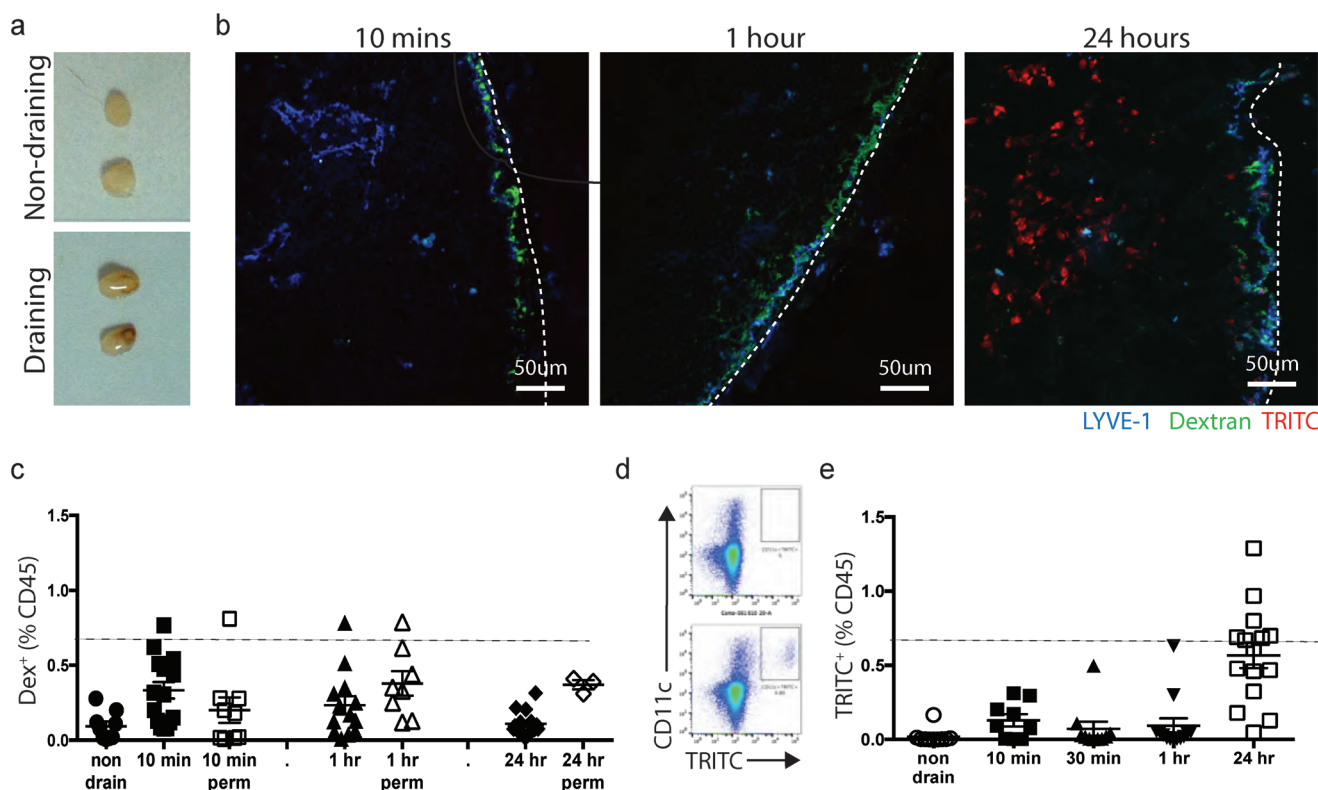
**ADVANCED
SCIENCE NEWS**

www.advancedsciencenews.com

NANO · MICRO

small

www.small-journal.com

Figure 1. Mechanical transport drives rapid SPIO nanoparticle drainage to the lymph node, by a cell-independent mechanism. a) Macroscopic analysis of non draining and SPIO-draining lymph nodes. b) Representative confocal images of draining lymph nodes 10 min, 1 h, and 24 h after SPIO and TRITC administration. TRITC-labeled dendritic cells (red); carboxydextran-coated SPIOs (dextran, green); LYVE-1 lymphatic structures (blue). Dashed lines indicate tissue edge. Scale bar, 50 µm. c) Flow cytometry quantification of dendritic cells with associated SPIO particles (expressed as a percentage of total CD45) 10 min, 1 h, and 24 h after SPIO injection. Cells were also permeabilized to measure internalized SPIO. d) Representative flow cytometry plot of TRITC-labeled dendritic cells (CD11c+) in non draining and draining lymph nodes 24 h after SPIO injection. e) Flow cytometry analysis of migratory dendritic cells 10 min, 30 min, 1 h, and 24 h after SPIO injection and topical application of TRITC; Data presented as mean ± SEM. Graphs represent data from three independent experiments. Each symbol represents a lymph node. ****$P < 0.0001$, one-way ANOVA with Tukey posthoc test.

sensitizing agents to permeate the epidermis and be engulfed, dendritic cells (DCs) were isolated from age-matched C57BL/6 mice, live-labeled, and coinjected sub-cutaneously with SPIO to directly compare the kinetics of dendritic cell and SPIO homing. As described earlier, SPIO were observed within the LNs at the earliest time points measured and were still apparent 24 h later. By contrast, and consistent with the earlier TRITC painting data, labeled DCs could only be detected within LN 24 h after inoculation (Figure S1c, Supporting Information). This was consistent with earlier TRITC paint data and indicated that rapid SPIO arrival at the SLN was independent of cellular processes, and was not a result of DC trafficking missed or underestimated due to limitations of the technique.

2.2. Long-Term SPIO Dynamics

Having measured the acute kinetics of SPIO transport and localization in draining LNs, we next sought to characterize longer-term localization and accumulation both at the injection site (ears, **Figure 2**a) and LNs (Figure 2b). Immediately postinjection, the carboxydextran coating of SPIO was observed diffusely within the tissue consistent with free solution from the injection bolus. Similarly, iron of the particle core was also dispersed

throughout the injection site (Figure 2a, blue, right panel). Seven days post injection, the carboxydextran coating was still detectable within tissue, but to a lesser extent than T0 (Figure 2a, left panel), however, iron remained diffused within the dermis. By one month, carboxydextran was no longer detectable at the injection site, although iron was still clearly identifiable. This remained the case even one year after injection (Figure 2, right panels) indicating that long-term, iron was retained within resident phagocytic cells once the coating had been digested. This was also true in LNs draining the injection site, with more punctate, cellular patterns of localization still observed at one year (Figure 2b; Figure S1a, Supporting Information). However, while iron remained visually abundant within tissues, quantification of levels using the Sentimag probe showed that relative iron content was indeed decreasing with time (Figure 2c). During this long-term analysis, we assumed that particles likely accumulated in macrophage rich areas (Figure 2a,b).

2.3. Impact of SPIO on Macrophage Cell Line Phenotypes

Given that macrophages are important components of the innate immune system, we proceeded to determine the potential impact of SPIO accumulation on macrophage phenotype
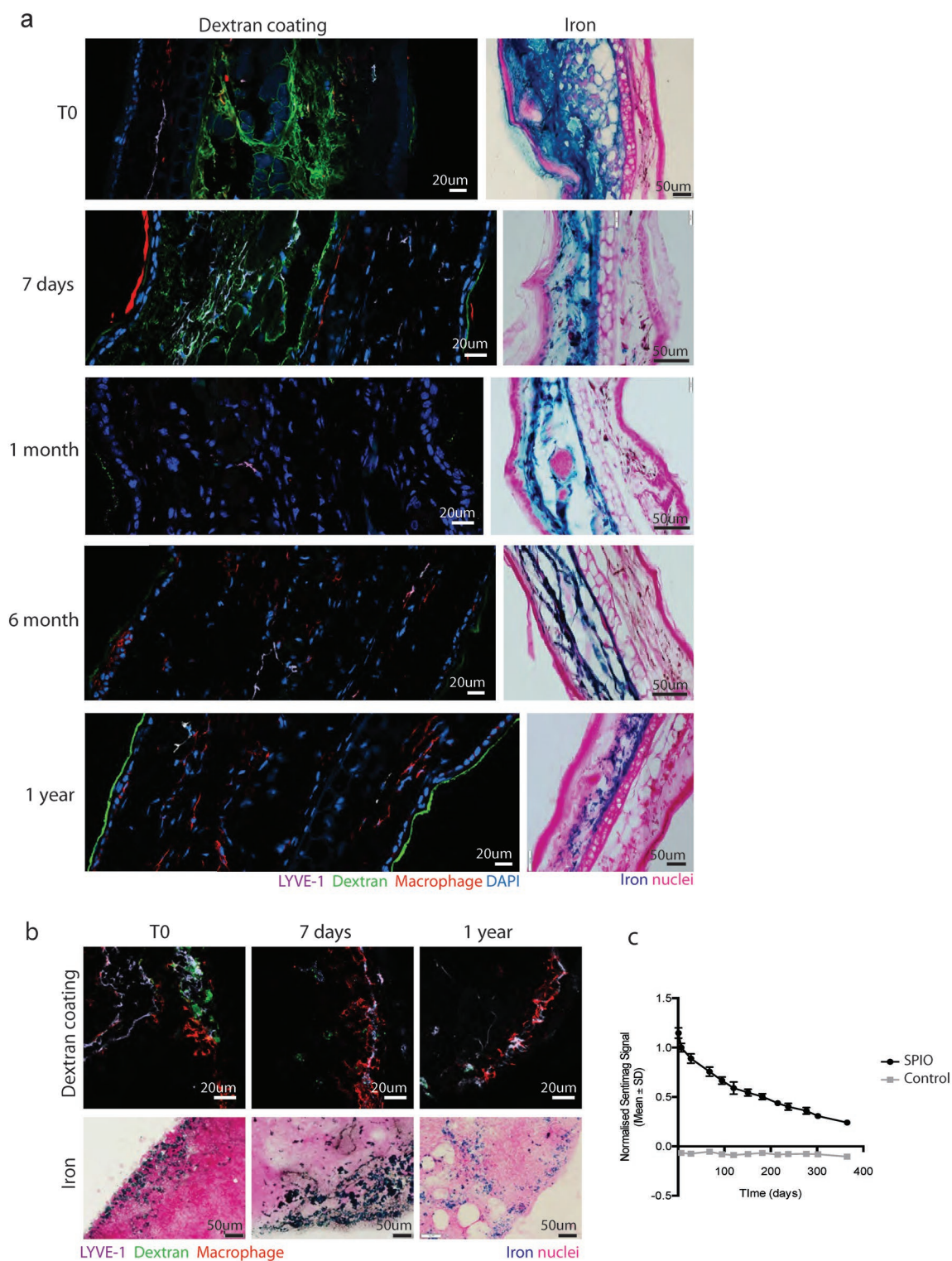
ADVANCED
SCIENCE NEWS
www.advancedsciencenews.com

NANO · MICRO
small
www.small-journal.com

Figure 2. SPIOs show long-term retention in local tissue. a) Representative images of SPIO at the injection site from 10 min to 1 year. Left panels: confocal images of injection site showing dextran coating (LYVE-1, pale purple; carboxydextran-coating of SPIO, green; macrophage, red; DAPI, blue), scale bar: 20 μm. Right panels: brightfield imaging of injection site showing iron (Perl's stain) counterstained with pararosaniline. Scale bar: 50 μm. b) Representative images of SPIO at the draining lymph node from 10 min to 1 year post injection. Top panels: confocal images of lymph node showing dextran coating (LYVE-1, pale purple; carboxydextran-coating of SPIO, green; macrophage, red). Dashed lines indicate tissue edge. Scale bar: 20 μm. Lower panels: brightfield imaging of lymph node showing iron (Perl's stain) counterstained with pararosaniline. Scale bar: 50 μm. c) Quantification of iron signal at injection site (black symbols) using the SentiMag probe, over the course of a year. Age matched control animals (grey symbols) did not receive injections. Data presented as normalized mean ± SD. $n = 11$ SPIO injected animals and 9 control animals.

and function in vitro, using two widely used macrophage cell lines: J774.2 and RAW264.7. First, we examined the uptake of nanoparticles (**Figure 3**a; Figures S2a,b and S3a, Supporting Information) using two different iron concentrations for the assays, 0.1 and 1 mg mL^{-1}, where the macrophages were saturated (Figure S2a,b, Supporting Information). As a comparison, 60 nm gold nanoparticles were used. As expected, both cell lines readily engulfed SPIO particles, and an increasing cargo was accompanied by an increase in the macrophage side scatter area (SSC-A) as measured by flow cytometry (Figure 3a; Figures S2a,b and S3a, Supporting Information) and imaging (Figure 3b; Figure S3b, Supporting Information). To recapitulate the acute versus persistent effects that these particles may have in the macrophages, cells were analyzed 1 and 7 days after
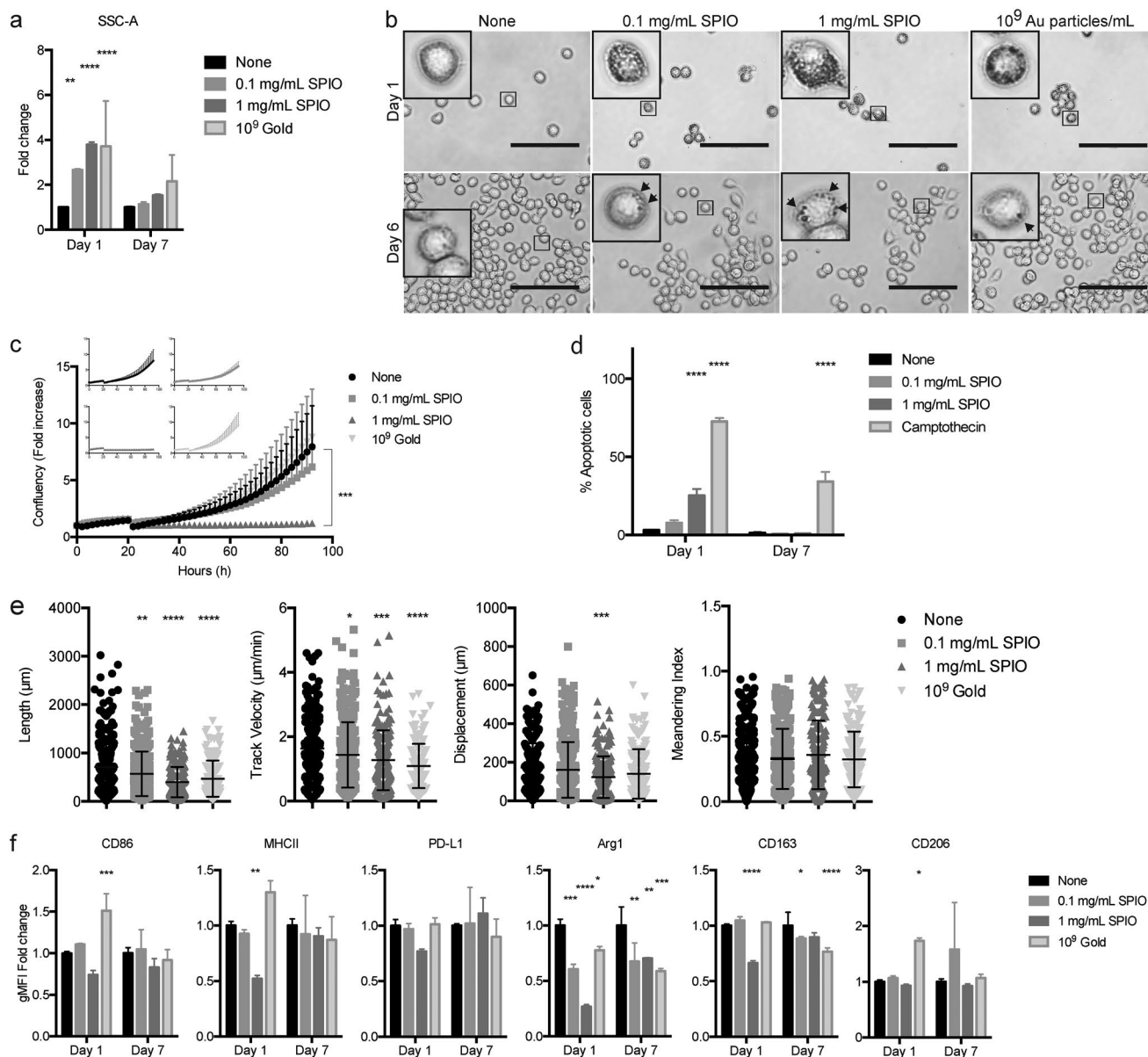

Figure 3. SPIO nanoparticles induce transient effects on J774.2 macrophage behavior. a) Dose dependent shift in macrophage granularity measured by SSC-A following incubation with SPIO or gold nanoparticles, measured 1 or 7 days after incubation. b) Representative brightfield images of J774.2 macrophages after incubation with SPIO at varying concentrations and gold nanoparticles. Images taken at days 1 and 6. Insets show higher magnification region of interest. Arrows indicate nanoparticles within cells. Scale bar: 100 μm. c) Growth curve for macrophages in contact with SPIO and gold nanoparticles, measured every two hours for 90 h. Data presented as fold increase in confluency. d) Percent of apoptotic cells measured by flow cytometry 1 and 7 days after incubation with SPIO and gold nanoparticles determined by Annexin V/7-AAD staining. Camptothecin was used as a positive control for apoptosis. e) Quantification of random cell motility after incubation with SPIO and gold nanoparticles. Cells were tracked for 24 h and parameters of length, track velocity, displacement, and meandering index were measured. f) Quantification of markers of macrophage polarization at days 1 and 7 after exposure to SPIO and gold nanoparticles. M1 markers; CD86, MHCII, and PD-L1. M2 markers; Arg1, CD163, and CD206. Data presented as mean ± SD. All graphs are combined data from at least two experiments performed in triplicate. *$p < 0.05$, **$p < 0.01$, ***$p < 0.001$, ****$p < 0.0001$ (two-way ANOVA with Tukey posthoc test; in (e) one-way ANOVA with Tukey posthoc test).

incubation with SPIO. By day 7, the SSC-A of cells returned to baseline, which implied that macrophages either secrete digested SPIO (iron aggregates, which we did not observe) or they simply divide their iron content between daughter cells.

We next sought to assess the influence of SPIO on proliferation, apoptosis, migration, and polarization in vitro (Figure 3), since functional defects in homing and immune responsiveness resulting from long-term accumulation may be clinically detrimental. When saturated with iron particles, a decrease in proliferation over 96 h was observed (Figure 3c; Figure S3c, Supporting Information), and this was accompanied by a transient increase in apoptosis, which returned to baseline levels by day 7 (Figure 3d; Figure S2d, Supporting Information). Similar behavior has been described for Kupffer cells upon uptake of Ferucarbotran SPIO particles.[45] By contrast, 0.1 mg mL^{-1} had no significant impact on proliferation or cell death. An important note here was that the lower iron concentration used in vitro was still 56 times greater than the dosage used in the clinical setting. 24 h after uptake of SPIO particles, a decrease in the random migration parameters was observed with increasing concentration (Figure 3e; Figure S3e, Supporting Information), but this was not unexpected since loaded cells were larger, they would require time to process their cargo and also require more energy to drag payloads. In light of recent studies that reported a shift in macrophage polarization upon iron nanoparticle uptake,[40,41,46] we sought to determine whether SPIO impacted polarization, and potentially determine changes in downstream immune function, examining typical surface markers characteristic of proinflammatory M1 (CD86, PD-L1, MHCII) and immunosuppressive M2 (Arginase 1, CD163, CD206/Mannose receptor) phenotypes. Earlier reports indicated that nanoparticles transiently shifted M2 macrophages toward an M1-like phenotype in both disease free[41] and tumor settings.[40,46] Cells saturated with SPIO particles displayed a transient decrease in MHCII and CD163 returning to control levels by day 7, while both concentrations of SPIO reduced arginase levels (Figure 3f; Figure S3f, Supporting Information). Interestingly, gold nanoparticles induced CD86 and MHC levels indicative of maturation and activation. Although we observed a transient reduction in M2-associated markers, no clear shift in phenotype toward M1 was detected (Figure S2c, Supporting Information). We also analyzed the effect of the low molecular weight carboxydextran-coating of SPIO nanoparticles and saw that it alone was sufficient to promote similar transient shifts in surface markers on both cell lines tested (Figure S2d,e, Supporting Information). In contrast to previous reports that focused on acute effects of particles on macrophage behavior, we also evaluated the longer-term effects. And while these indicated some immediate effects, changes were transient with macrophages recovering normal behavior by day 7. This was consistent with data showing skin macrophage populations renew every 4 to 9 days,[47,48] and could account for the "dilution" of any initial effects.

we examined characteristics including phagocytosis, antigen-presentation, and cytokine production. Phagocytosis capacity was quantified using 1 μm Fluoresbrite fluorescent microspheres (to mimic bacteria or debris, **Figure 4**a) before and after incubation with SPIO. Again, we observed a transient decrease in phagocytic ability when macrophage cell lines received high concentrations of SPIO nanoparticles (Figure 4b; Figure S4a, Supporting Information), which was not surprising since cells were saturated and at full capacity. Having tested different concentrations of iron, cells were unable to uptake more iron in the presence of concentrations above 1 mg mL^{-1} (Figure S2a, Supporting Information). Phagocytosis returned to control levels at later time points. Interestingly, the gold nanoparticles induced no change in bead uptake, which could reflect that macrophages were not saturated with the gold particles. We then sought to determine capacity to uptake and process antigen in the forms of TRITC-labeled ovalbumin (OVA) and DQ-OVA. An initial decrease in the uptake of TRIC-OVA was recorded compared with control, but this recovered by day 7 (Figure 4c; Figure S4b, Supporting Information). Despite a significant reduction in antigen uptake of ≈80% shortly after incubation, proteolytic processing was only reduced by 30% with 0.1 mg mL^{-1}, indicating that although sampling may have been transiently impaired, the downstream processing pathways to antigen presentation remained intact Figure 4d; Figure S4c, Supporting Information).

Previous studies considered the effects SPIO in the absence of an inflammation insult.[38,41,44–46] However, due to the importance of macrophage functionality during inflammation, we also induced inflammation after incubation with SPIO to determine if the particles had any impact on responses. Because macrophages can modulate immune responses through their secretome, we analyzed cytokine production of both cell lines using a LEGENDplex multianalyte flow assay after SPIO uptake before and after an immune insult with LPS (**Figure 5**; Figure S5, Supporting Information). The vast majority of the cytokines examined showed no significant differences under baseline conditions. The addition of LPS induced differential production of some cytokines (red boxes), although again, with the exception of IL-1 and IL-10, it was inflammation rather than the presence of particles that induced these changes. This would imply that particle-loaded cells were still capable of responding to inflammatory insults. Interestingly, the increase observed at late time points with IL-1 and concurrent decrease in IL-10 indicated a more functionally activated phenotype. At the same time, an increase in IL-27 with increasing payload may have been indicative of an attempt to boost IL-10 and regulate proinflammatory cytokine production.[49–51] We did not see an SPIO specific induction of M1 or M2 signatures following LPS induction of inflammation. Further analysis of polarization and phagocytosis capacity was also consistent with our previous analysis (Figures 3 and 4; Figures S3 and S4, Supporting Information) in the presence or absence of an inflammation insult (Figures S6 and S7, Supporting Information).

2.4. Impact of SPIO on Macrophage Cell Line Function In Vitro

While surface marker expression provides some indication of responses to particle uptake, functional outputs are more informative when considering potential long-term clinical impact. Thus,

2.5. Impact of SPIO on Macrophage Function In Vivo

As the doses in vitro far exceeded those experienced in vivo, even at the lowest concentration tested, we analyzed the impact
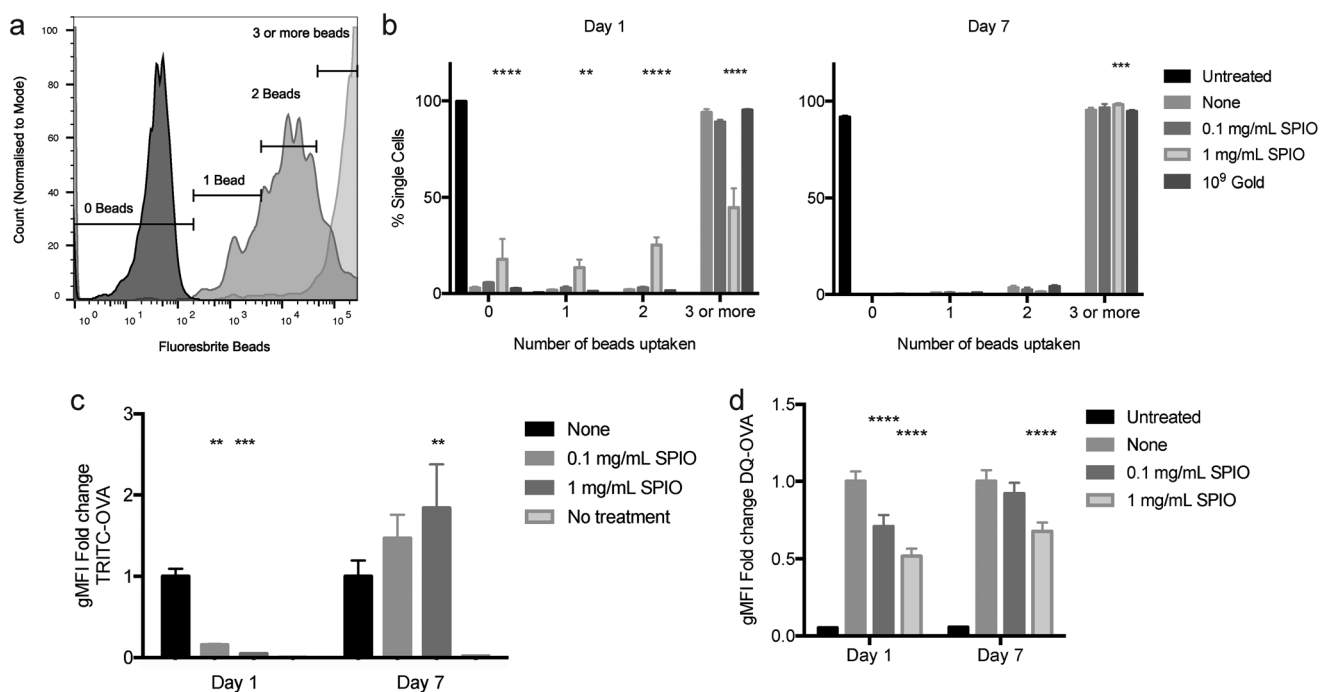
Figure 4. SPIO nanoparticles induce transient functional changes on J774.2 macrophages. a) Schematic representation of the flow cytometry profiles measuring the phagocytic uptake of fluorescent microbeads. Phagocytic capacity of b) 1 µm Fluoresbrite YG beads and c) TRITC-OVA soluble antigen following SPIO exposure was quantified at days 1 and 7. d) Antigen processing ability of macrophages assessed by the cleavage of DQ-OVA at days 1 and 7 after SPIO exposure. Data presented as mean ± SD. All graphs combine data from at least two experiments performed in triplicate. $*p < 0.05$, $**p < 0.01$, $***p < 0.001$, $****p < 0.0001$ (two-way ANOVA with Tukey posthoc test).

of SPIO particles in macrophages in vivo at both the injection site (receiving a higher dose) or in the draining LN over time. There were no differences in immune cell populations at either site following inoculation (**Figure 6**a,b), but we detected dextran+ macrophages at the injection site that had taken up nanoparticles immediately following injection (Figure 6b). This was not the case at the LN, or at later time-points, consistent with previous data examining transport kinetics and dextran versus iron retention (Figures 1 and 2). At the draining LN, no significant alterations in macrophage phenotype were measured at any time point examined following SPIO injection (Figure 6c). At the injection site, decreased levels of PD-L1, Arg1, CD163, and CD208 were observed, as with in vitro assays, but these returned to levels comparable with controls by day 8 (Figure 6d) indicating no long-term changes in macrophages at either site following SPIO administration.

3. Conclusion

Carboxydextran-coated SPIO particles have recently been implemented as reliable alternatives to radioisotopes for intraoperative mapping and identification of sentinel LNs in cancer staging.[8,10–13] However, the mechanisms of transport to LNs and longer-term impact of tissue accumulation remained unclear. Here we identified that rapid transport to LNs was governed by mechanical rather than cell-mediated means[25–31] with SPIO detected in draining LN 10 min post administration, and localizing predominantly with lymphatic structures.

By contrast, cell-driven trafficking to lymph nodes required 24 h. We also demonstrated that, consistent with previous reports,[37,39–44] alterations in macrophage behavior could be observed immediately after exposure. However, these changes were transient, resolving to baseline levels by day 7. Moreover, macrophages retained the capacity to proteolytically process antigen and respond to an inflammatory stimulus following exposure to SPIO.[52] Thus, these data provide evidence to suggest that after an initial perturbation, carboxydextran-coated SPIO nanoparticles persisting within macrophages conferred no long-term disruption to macrophage phenotype or function.

4. Experimental Section

In Vivo Time-Course for Lymph Node Drainage Analysis—TRITC Paint versus SPIO, and In Vivo Iron Measurements: All in vivo experiments were performed with UK Home Office authority under Project Licenses 80/2574 and P88378375. TRITC and SPIO (Magtrace, Endomagnetics, Ltd, previously branded as Sienna+) solutions were prepared under sterile conditions. 10 mg TRITC was diluted in 1:1 mixture of acetone and dibutylphthalate (500 µL of each) to give final concentration of 10 mg mL^{-1}. Immune competent C57BL/6 mice were anaesthetized using 150 µL anesthetic stock solution (stock: 0.5 mL (50 mg) ketamine + 0.25 mL (5 mg) xylazine + 4.25 mL saline. Once asleep, any hair was removed using clippers. Then 25 µL of TRITC solution was slowly applied to the skin surface and gently spread using the pipette tip. Immediately following TRITC application, 10 µL of SPIO was injected sub-cutaneously to each site. Cages were placed in a temperature-controlled Vetbed during the recovery period. Applications of TRITC and SPIO were performed for time points of 10 min, 30 min, 1 h, 2 h, and 24 h. After 10 min,
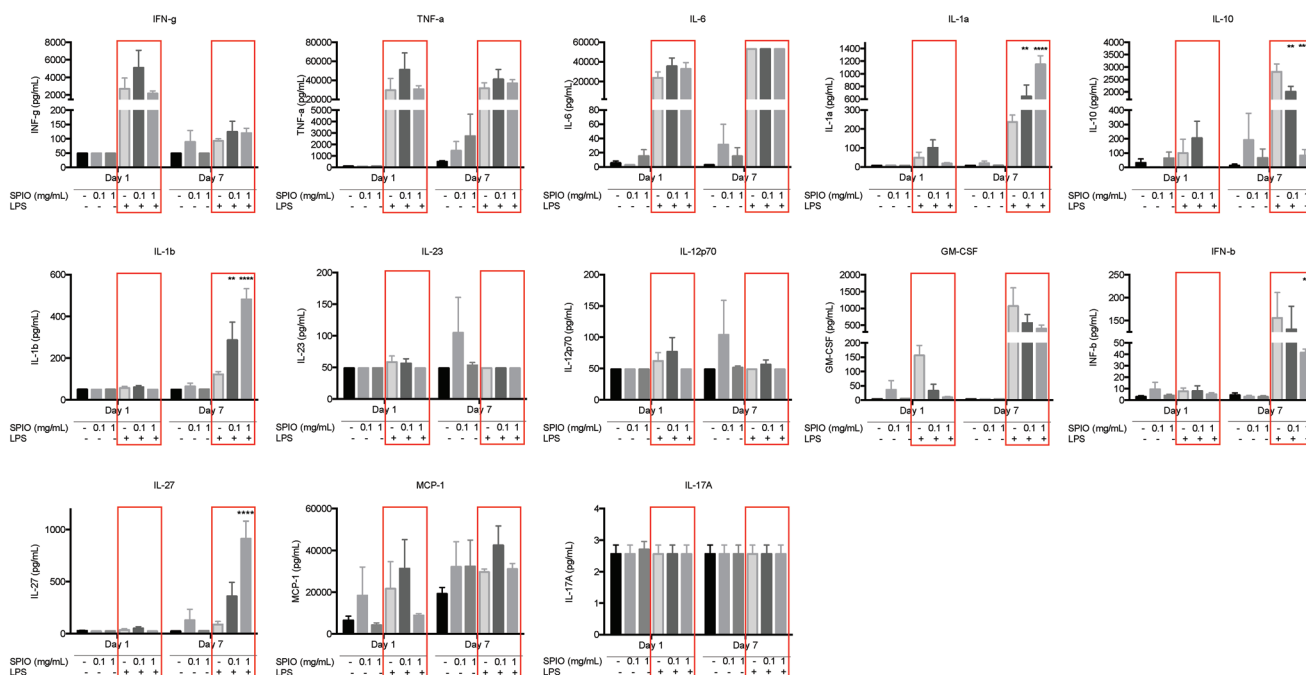
Figure 5. SPIO treated macrophages retain capacity to respond to inflammation. Supernatants from macrophage cell line cultures were collected at days 1 and 7 after no 0.1 or 1 mg mL⁻¹ SPIO treatment and analyzed for cytokine production using a multianalyte flow cytometry assay. Cytokine levels were measured with or without LPS inflammatory stimulus post SPIO. Quantification of CCL2 (MCP-1), GM-CSF, IFN-beta, IFN-gamma, IL-1 alpha, IL-1 beta, IL-6, IL-10, IL12 (p70), IL-17A, IL23, IL-27, TNF-alpha for each SPIO concentration. Red box indicates conditions under inflammation. Data presented as mean ± SEM from two experiments performed in triplicate. **$p < 0.01$, ****$p < 0.0001$ (two-way ANOVA with Tukey posthoc test).

animals were euthanized using CO_2 followed by cervical dislocation. Draining LNs (brachial, for shoulder injections; and superficial cervical, for ear injections) were transferred to tubes containing sterile phosphate buffered saline (PBS) for cell isolation and flow cytometric analysis or snap frozen in optimal cutting temperature (OCT) cryo preservative using dry ice for tissue sections. Non draining inguinal nodes were also collected. These steps were repeated for all other time points. For long-term tracing, SPIO was injected on mice ears and iron content monitored for a year using a hand-held probe (Sentimag, Endomagnetics Ltd., Cambridge, UK). Note that a human dose of SPIO is on average 32 µmol iron kg⁻¹ (this was calculated considering that humans get 112 mg of iron per injection and considering an average body weight of 62 kg). For these animal experiments, a 250 µmol iron kg⁻¹ dose was applied, over 7.8 times higher than in humans (considering an average mouse weight of 20 mg).

In Vivo Macrophage Depletion: 5 days prior to the time course assay, 200 µL clodrosome liposome suspension (liposomal formulation of clodronate, Encapsula Nanosciences) or control liposomes were injected via the intraperitoneal route into immune competent C57BL/6 mice. This was repeated 3 days later. Macrophage depletion was confirmed by flow cytometry. On day 0, SPIO was administered as described above, and LNs were collected at time points of 10 min, 1 h, and 24 h.

Isolation and Injection of Pre-labeled Dendritic Cells: CD11c+ dendritic cells were harvested from spleens. Briefly, under sterile conditions, spleens were gently teased apart with 25G needles and enzymatically dissociated with 1 mg mL⁻¹ collagenase D (Roche). Following incubation at 37 °C for 30 min, the enzymatic reaction was stopped with ethylenediaminetetraacetic acid (EDTA). The resulting cell suspension was passed through 70 µm nylon mesh to remove large debris. Erythrocytes were then removed by treatment with ammonium chloride solution (0.15 M NH_4Cl, 1×10^{-3} M $KHCO_3$, 0.1×10^{-3} M EDTA) for 5 min at room temperature. After centrifugation at 1200 rpm for 6 min, the splenocyte cell pellet was resuspended in magnetic activated cell sorting (MACS) buffer (PBS containing 2×10^{-3} M EDTA and 0.5% bovine serum albumin (BSA)). CD11c+ dendritic cells were then positively selected using CD11c+ magnetic microbeads (Mitenyi Biotec)

according to manufacturer's guidelines. Once collected, dendritic cells were live-labeled. Cells were incubated in 1×10^{-6} M CellTracker Red CMTPX (Molecular Probes) for 10 min at 37 °C and were then allowed to recover for 30 min in full Roswell Park Memorial Institute (RPMI) media supplemented with 10% fetal bovine serum (FBS) and 1% penicillin/streptomycin. Cells were counted and pelleted. Purity and viability of cells was confirmed by flow cytometry. Upon successful anaesthetization of mice, the cells were mixed with SPIO working solution and sub-cutaneous coinjection was performed as described above.

Immunofluorescence: Harvested LNs were embedded in OCT cryo-preservative and sliced into 10 µm sections using a cryostat. Sections were air dried and stored at −80 °C and were then subjected to standard immunofluorescence protocols. Briefly, slides were fixed in ice-cold acetone for 2 min at −20 °C, then washed in PBS. This was followed by a blocking step, incubating samples in 10% chicken serum in PBS/0.5% BSA for 30 min, room temperature. Sections were incubated in primary antibody combinations (1:20 for dextran, 1:100 for macrophages, 1:300 for LYVE-1; see figure legends and Table S1 (Supporting Information) for list of antibodies and suppliers) overnight at 4 °C. Primary antibodies were removed with three PBS washes and appropriate fluorescently conjugated secondary antibodies (at a 1:300 dilution) were added (45 min, room temperature in the dark). Slides were washed, coverslipped with Vectashield liquid mounting media (Vectorlabs), and sealed with nail polish. Sections were imaged using a Zeiss LSM 510 Meta confocal microscope and final, merged-channel images were generated using Image J software.

Iron Oxide Detection: LNs were subjected to standard immunohistochemistry protocols. Briefly, slides were rehydrated in PBS before endogenous peroxidases were blocked using 3% hydrogen peroxide for 5 min. Samples were then subjected to a non-immune block and incubated in blocking buffer (10% chicken serum in PBS/2% BSA) for 30 min, at room temperature. Blocking buffer was removed and replaced with primary antibody solution containing anti-mouse LYVE-1 (Abcam, 1:300 dilution) for 3 h at room temperature. Samples were washed three times followed by a second non-immune block. Biotinylated anti-rabbit secondary antibody (1:300 dilution) was then
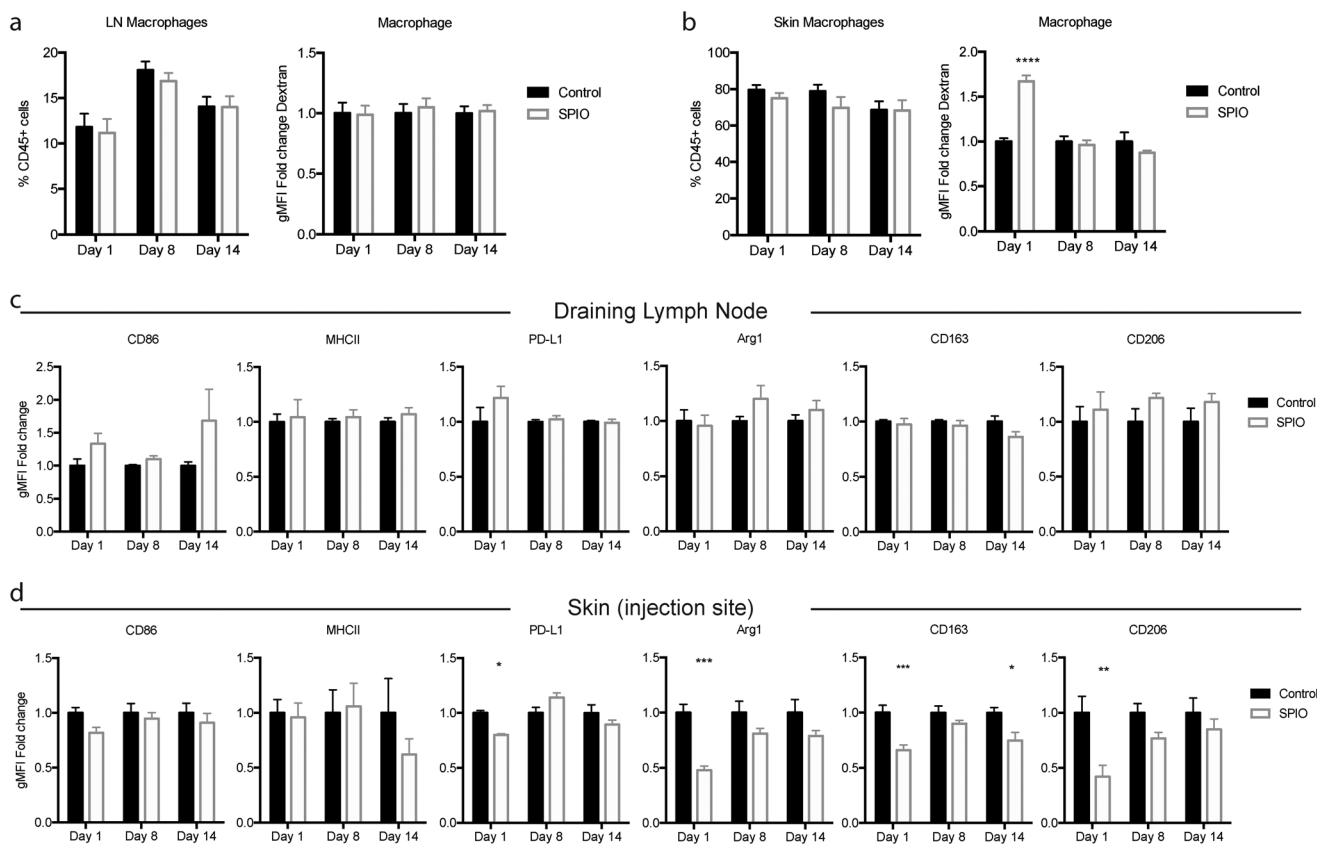
Figure 6. SPIO nanoparticles induce transient phenotypic changes to the macrophage compartment in vivo. a) Percent of macrophages within the immune compartment of lymph nodes at days 1, 8, and 14 after SPIO injection. Right: relative macrophage uptake of dextran-coated SPIO. b) Percent of macrophage cells in the immune compartment at the injection site (skin) at days 1, 8, and 14 after SPIO injection. Right: relative macrophage uptake of dextran-coated SPIO. c) Expression of polarization markers by lymph node macrophages after SPIO injection measured by flow cytometry at days 1, 8, and 14. Classical M1 markers: CD86, MHCII, and PD-L1. Classical M2 markers: Arg1, CD163, and CD206. d) Expression of polarization markers by skin macrophages at the site of injection after SPIO injection, measured by flow cytometry at days 1, 8, and 14. Classical M1 markers: CD86, MHCII, and PD-L1. Classical M2 markers: Arg1, CD163, and CD206. Data presented as mean ± SEM from two experiments performed in triplicate. **$p < 0.01$, ****$p < 0.0001$ (two-way ANOVA with Tukey posthoc test).

added to each section and incubated for 30 min at room temperature. Meanwhile, Avidin-Biotin Complex (ABC) solution (Vectorlabs) was prepared as per manufacturers guidelines. Samples were washed and the pre-prepared ABC solution was added and left on samples for 30 min. Following PBS washes, the peroxidase-based substrate solution was prepared and added as per manufactures guidelines (Vectorlabs). At this point, samples were closely watched for the development of a brown color resulting from the inclusion of 3,3′-diaminobenzidine in the substrate solution. When sufficient color developed, the reaction was stopped in miliQ water. Nuclei were counterstained with hematoxylin (Sigma). SPIO was then detected using a commercially available iron stain kit following manufacturers guidelines (Sigma). Sections were imaged using an Olympus BX53 brightfield microscope.

Flow cytometry—Tissues: Harvested LNs were gently teased apart with 25G needles and enzymatically dissociated with 1 mg mL^{-1} collagenase D (Roche). Following incubation at 37 °C for 30 min, the enzymatic reaction was stopped with EDTA. The resulting cell suspension was passed through 70 µm nylon mesh to remove large debris. Samples were transferred to a round bottom 96 well plate where staining was performed. Dead cells were excluded using live/dead violet fixable stain (as per manufacturers guidelines; Molecular Probes). Surface antigens were stained with appropriate fluorescently conjugated primary antibodies (all 1:300 dilution), incubating for 30 min on ice in the dark. Biotinylated antibodies were detected with conjugated streptavidin (1:300 dilution) for 30 min on ice in the dark. In cases where intracellular staining was required, i.e., to demonstrate that SPIO was not notably

internalized, samples were fixed and permeabilized using a FoxP3 staining kit (eBiosciences) as per manufacturers guidelines, and then incubated for a second time with FITC-conjugated anti-dextran antibody (30 min on ice in the dark). Please refer to Table S1 (Supporting Information) for list of antibodies and suppliers. Data were then collected on a CyAn ADP Analyzer flow cytometer (Beckman Coulter) and analyzed using FlowJo software (Treestar).

Cell Culture and Nanoparticle Incubation: J774.2 (purchased from Culture Collections, Public Health England) and RAW264.7 (kindly provided by Ellen Gokkel) macrophage cell lines were cultured in Dulbecco's modified Eagle's medium containing 4.5 g L^{-1} of glucose supplemented with 10% fetal calf serum. Cells were split and incubated with SPIO for 24 h, at two different concentrations (0.1 and 1 mg mL^{-1}) and were then thoroughly washed with PBS before subsequent functional analysis. NB; a human dose of SPIO is on average 32 µmol iron kg^{-1}. Here, the 0.1 and 1 mg mL^{-1} doses were equivalent to 1.79 µmol iron mL^{-1} (1.79 mol kg^{-1}—56 times more than in humans) and 17.9 µmol iron mL^{-1} (17.9 mol kg^{-1}—556 times more than in humans), respectively. As a control, gold nanoparticles (60 nm, Sigma) were used at a concentration of 4×10^9 particles mL^{-1}. Analyses were performed at 24 h and 7 days. Nanoparticle uptake was detected by the increase in granularity of the cells, which directly correlates to the increase of the side scatter (SSC-A) of the cells when analyzed by flow cytometry.

Inflammation Induction: Macrophages (in presence or absence, or previously incubated with SPIO) were incubated for 24 h with LPS (bacterial lipopolysaccharide, 100 ng mL^{-1}) and interferon (IFN)-gamma

**ADVANCED
SCIENCE NEWS**

www.advancedsciencenews.com

NANO · MICRO

small

www.small-journal.com

(20 ng mL^{-1}) to induce inflammatory response. Cytokine production and phagocytosis ability were then assessed.

Phagocytosis Assay: Large particle phagocytosis ability of macrophages was assessed using 1 µm fluorescent particles (Fluoresbrite YG beads, Polysciences Inc.). Particles were vigorously vortexed and added (1:20 dilution) to a macrophage cell suspension and were then incubated for 20 min at 37 °C and 5% CO$_2$. Suspensions were washed with PBS and then treated with 0.2% Trypan blue for 3 min and immediately diluted 1:1 in PBS. Two final washes preceded analysis by flow cytometry for particle content. Soluble uptake of antigen was assessed using soluble TRITC (Tetramethylrhodamine)-conjugated ovalbumin (TRITC-OVA, Invitrogen). Macrophages were incubated with 100 µg mL^{-1} of TRITC-OVA for 30 min. Cells were then washed with ice-cold PBS containing 5% FBS. A final wash with PBS was performed before flow cytometry analysis.

Macrophage Polarization Analysis—Flow Cytometry: Flow cytometry was used to analyze the expression of M1 (proinflammatory: MHCII, PD-L1, CD86) and M2 markers (anti-inflammatory: Arginase 1, CD163, CD206) on cultured macrophages. Cells were scraped from the wells following treatments and washed with PBS, and were then incubated with antibodies for the identification of surface markers for 20 min at a dilution of 1:200 (primary antibodies) or 1:300 (secondary antibodies). Cell suspensions were then fixed and permeabilized using a fixation/permeabilization kit (eBiosciences) and probed for the presence of intracellular Arg1. Please refer to Table S1 (Supporting Information) for list of antibodies and suppliers. Data were acquired using a Fortessa (BD) flow cytometer and analyzed using FlowJo.

DQ-OVA Assay: DQ-OVA (Invitrogen) was used to determine the ability of macrophage to digest uptaken antigen. Macrophages were incubated with 100 µg mL^{-1} of DQ-OVA for 15 min at 37 °C, washed three times with ice-cold PBS containing 5% FBS, and immediately analyzed by flow cytometry to analyze the presence of the fluorescent product resulting from DQ-OVA digestion.

Cytokine Production—Flow Cytometry: Supernatants from macrophage cultures at different time points (at days 1 and 7) were collected for cytokine production analysis using the LEGENDplex kit (Biolegend). Detection of CCL2 (MCP-1), GM-CSF, IFN-beta, IFN-gamma, IL-1 alpha, IL-1 beta, IL-6, IL-10, IL-12 (p70), IL-17A, IL-23, IL-27, and TNF-alpha was performed by flow cytometry.

Proliferation: Cells were seeded in a 12-well plate and proliferation was calculated by following the percent confluency of the well using Incucyte Zoom (Essen BioScience) Live Cell analysis system. Images were acquired every two hours for a total of 90 h.

As a confirmation, methodology cells were seeded in a 12-well plate and counted using the trypan blue exclusion method.

Apoptosis: Cells were assayed in 96-well round bottom plates. After treatment, samples were washed with cold PBS twice and then resuspended in 100 µL of Annexin V Binding Buffer (cat # 422 201, Biolegend). 5 µL of FITC Annexin V (Biolegend) and 5 µL of 7-AAD (cat # 420 403, Biolegend) were then added to each well. Samples were incubated in the dark for 15 min at RT (20 °C). 100 µL of Annexin V Binding Buffer was then added to each well and analyzed by flow cytometry. As a positive control, macrophages were incubated with 6×10^{-6} M of Camptothecin (Acros Organics) for 6 h prior to Annexin V/7-AAD staining.

Cellular Random Migration Analysis: Macrophage cell lines were seeded in 8-well chamber slides and placed in a microscope (Zeiss Axio Observer.Z1 coupled with incubation chamber) where their behavior was followed by acquiring images every 20 min for a total of 24 h. Migration analysis was performed using Volocity software (Perkin Elmer).

Imaging: Bright field images of the different macrophage cell lines were collected using an EVOS (Thermo Fisher) system at days 1 and 6.

Statistical Analysis: Statistical analyses were performed using GraphPad Prism 6 software (GraphPad). For comparisons of two groups, Students *t*-tests were performed. When comparing three or more datasets, one-way ANOVA and appropriate posthoc tests were performed as described in figure legends.

Supporting Information

Supporting Information is available from the Wiley Online Library or from the author.

Conflict of Interest

Quentin Harmer is the CTO at Endomagnetics Ltd. and Eric Mayes is the CEO at Endomagnetics Ltd. The other authors declare that they do not have any conflict of interest.

[1] Q. A. Pankhurst, N. T. K. Thanh, S. K. Jones, J. Dobson, *J. Phys. D: Appl. Phys.* **2009**, *42*, 224001.

[2] H. Zhang, X. L. Liu, Y. F. Zhang, F. Gao, G. L. Li, Y. He, M. L. Peng, H. M. Fan, *Sci. China: Life Sci.* **2018**, *61*, 400.

[3] K. J. Robinson, S. R. Corrie, K. J. Thurecht, J. Islam, D. Bobo, *Pharm. Res.* **2016**, *33*, 2373.

[4] A. C. Anselmo, S. Mitragotri, *Bioeng. Transl. Med.* **2016**, *1*, 10.

[5] J. L. Campbell, J. V. Jokerst, P. Ghanouni, S. S. Gambhir, A. S. Thakor, E. Mittra, *J. Nucl. Med.* **2016**, *57*, 1833.

[6] C. L. Ventola, *P T.* **2017**, *42*, 742.

[7] H. E. Daldrup-Link, *Radiology* **2017**, *284*, 616.

[8] Y. X. J. Wáng, J.-M. Idée, *Quant. Imag. Med. Surg.* **2017**, *7*, 88.

[9] J. J. Pouw, M. R. Grootendorst, R. Bezooijen, C. A. H. Klazen, W. I. De Bruin, J. M. Klaase, M. A. Hall-Craggs, M. Douek, B. ten Haken, *Br. J. Radiol.* **2015**, *88*, 20150634.

[10] A. Karakatsanis, P. M. Christiansen, L. Fischer, C. Hedin, L. Pistioli, M. Sund, N. R. Rasmussen, H. Jørnsgård, D. Tegnelius, S. Eriksson, K. Daskalakis, F. Wärnberg, C. J. Markopoulos, L. Bergkvist, *Breast Cancer Res. Treat.* **2016**, *157*, 281.

[11] M. Douek, J. Klaase, I. Monypenny, A. Kothari, K. Zechmeister, D. Brown, L. Wyld, P. Drew, H. Garmo, O. Agbaje, Q. Pankhurst, B. Anninga, M. Grootendorst, B. Ten Haken, M. A. Hall-Craggs, A. Purushotham, S. Pinder, *Ann. Surg. Oncol.* **2014**, *21*, 1237.

[12] B. Anninga, M. Ahmed, M. Van Hemelrijck, J. Pouw, D. Westbroek, S. Pinder, B. Ten Haken, Q. Pankhurst, M. Douek, *Breast Cancer Res. Treat.* **2013**, *141*, 33.

[13] L. Johnson, S. E. Pinder, M. Douek, *Histopathology* **2013**, *62*, 481.

[14] M. Teshome, C. Wei, K. K. Hunt, A. Thompson, K. Rodriguez, E. A. Mittendorf, *Ann. Surg. Oncol.* **2016**, *23*, 1508.

[15] R. Weissleder, D. D. Stark, B. L. Engelstad, B. R. Bacon, D. L. White, P. Jacobs, J. Lewis, *Am. J. Roentgenol.* **1989**, *152*, 167.

ADVANCED
SCIENCE NEWS
www.advancedsciencenews.com

NANO · MICRO
small
www.small-journal.com

[16] O. V. Khullar, A. P. Griset, S. L. Gibbs-Strauss, L. R. Chirieac, K. A. V. Zubris, J. V. Frangioni, M. W. Grinstaff, Y. L. Colson, *J. Am. Coll. Surg.* **2012**, *214*, 328.

[17] V. Manolova, A. Flace, M. Bauer, K. Schwarz, P. Saudan, M. F. Bachmann, *Eur. J. Immunol.* **2008**, *38*, 1404.

[18] S. T. Reddy, *J. Appl. Physiol.* **2006**, *101*, 1162.

[19] C. Oussoren, J. Zuidema, D. J. A. Crommelin, G. Storm, *Biochim. Biophys. Acta, Biomembr.* **1997**, *1328*, 261.

[20] C. Oussoren, G. Storm, *Adv. Drug Delivery Rev.* **2001**, *50*, 143.

[21] S. T. Reddy, A. Rehor, H. G. Schmoekel, J. A. Hubbell, M. A. Swartz, *J. Controlled Release* **2006**, *112*, 26.

[22] S. T. Proulx, P. Luciani, S. Derzsi, M. Rinderknecht, V. Mumprecht, J. C. Leroux, M. Detmar, *Cancer Res.* **2010**, *70*, 7053.

[23] X. Cai, W. Li, C. H. Kim, Y. Yuan, L. V. Wang, Y. Xia, *ACS Nano* **2011**, *5*, 9658.

[24] D. Sen, T. J. Deerinck, M. H. Ellisman, I. Parker, M. D. Cahalan, *PLoS One* **2008**, *3*, e3290.

[25] G. J. Randolph, K. Inaba, D. F. Robbiani, R. M. Steinman, W. A. Muller, *Immunity* **1999**, *11*, 753.

[26] A. Braun, T. Worbs, G. L. Moschovakis, S. Halle, K. Hoffmann, J. Bölter, A. Münk, R. Förster, *Nat. Immunol.* **2011**, *12*, 879.

[27] R. Förster, A. Braun, T. Worbs, *Trends Immunol.* **2012**, *33*, 271.

[28] M. Rescigno, F. Granucci, S. Citterio, M. Foti, P. Ricciardi-Castagnoli, *Immunol. Today* **1999**, *20*, 200.

[29] K. Sato, Y. Imai, T. Irimura, *J. Immunol.* **1998**, *161*, 6835.

[30] K. Otero, A. Vecchi, E. Hirsch, J. Kearley, W. Vermi, A. Del Prete, S. Gonzalvo-feo, C. Garlanda, O. Azzolino, *Blood* **2010**, *116*, 2942.

[31] G. J. Randolph, J. Ochando, S. Partida-Sánchez, *Annu. Rev. Immunol.* **2008**, *26*, 293.

[32] C. C. Clement, O. Rotzschke, L. Santambrogio, *Trends Immunol.* **2011**, *32*, 6.

[33] J. E. Gretz, C. C. Norbury, A. O. Anderson, A. E. I. Proudfoot, S. Shaw, *J. Exp. Med.* **2000**, *192*, 1425.

[34] M. Sixt, N. Kanazawa, M. Selg, T. Samson, G. Roos, D. P. Reinhardt, R. Pabst, M. B. Lutz, L. Sorokin, *Immunity* **2005**, *22*, 19.

[35] H. Hillaireau, P. Couvreur, *Cell. Mol. Life Sci.* **2009**, *66*, 2873.

[36] O. Lunov, T. Syrovets, C. Loos, J. Beil, M. Delacher, K. Tron, G. U. Nienhaus, A. Musyanovych, V. Mailänder, K. Landfester, T. Simmet, *ACS Nano* **2011**, *5*, 1657.

[37] V. Kodali, M. H. Littke, S. C. Tilton, J. G. Teeguarden, L. Shi, C. W. Frevert, W. Wang, J. G. Pounds, B. D. Thrall, *ACS Nano* **2013**, *7*, 6997.

[38] D. A. Kedziorek, N. Muja, P. Walczak, J. Ruiz-Cabello, A. A. Gilad, C. C. Jie, J. W. M. Bulte, *Magn. Reson. Med.* **2010**, *63*, 1031.

[39] H. Unterweger, C. Janko, M. Schwarz, L. Dézsi, R. Urbanics, J. Matuszak, E. Őrfi, T. Fülöp, T. Bäuerle, J. Szebeni, C. Journé, A. R. Boccaccini, C. Alexiou, S. Lyer, I. Cicha, *Int. J. Nanomed.* **2017**, *12*, 5223.

[40] S. Zanganeh, G. Hutter, R. Spitler, O. Lenkov, M. Mahmoudi, A. Shaw, J. S. Pajarinen, H. Nejadnik, S. Goodman, M. Moseley, L. M. Coussens, H. E. Daldrup-Link, *Nat. Nanotechnol.* **2016**, *11*, 986.

[41] J. M. Rojas, L. Sanz-Ortega, V. Mulens-Arias, L. Gutiérrez, S. Pérez-Yagüe, D. F. Barber, *Nanomed.: Nanotechnol., Biol. Med.* **2016**, *12*, 1127.

[42] S. Klein, A. Sommer, L. V. R. Distel, J. L. Hazemann, W. Kröner, W. Neuhuber, P. Müller, O. Proux, C. Kryschi, *J. Phys. Chem. B* **2014**, *118*, 6159.

[43] T. H. Chung, J. K. Hsiao, M. Yao, S. C. Hsu, H. M. Liu, D. M. Huang, *RSC Adv.* **2015**, *5*, 89932.

[44] A. Laskar, J. Eilertsen, W. Li, X. M. Yuan, *Biochem. Biophys. Res. Commun.* **2013**, *441*, 737.

[45] O. Lunov, T. Syrovets, C. Röcker, K. Tron, G. Ulrich Nienhaus, V. Rasche, V. Mailänder, K. Landfester, T. Simmet, *Biomaterials* **2010**, *31*, 9015.

[46] Y. Wang, Y. X. Lin, S. L. Qiao, H. W. An, Y. Ma, Z. Y. Qiao, R. P. Y. J. Rajapaksha, H. Wang, *Biomaterials* **2017**, *112*, 153.

[47] A. Baranska, A. Shawket, M. Jouve, M. Baratin, C. Malosse, O. Voluzan, T.-P. Vu Manh, F. Fiore, M. Bajénoff, P. Benaroch, M. Dalod, M. Malissen, S. Henri, B. Malissen, *J. Exp. Med.* **2018**, *215*, 1115.

[48] D. Hashimoto, A. Chow, C. Noizat, P. Teo, M. B. Beasley, M. Leboeuf, C. D. Becker, P. See, J. Price, D. Lucas, M. Greter, A. Mortha, S. W. Boyer, E. C. Forsberg, M. Tanaka, N. van Rooijen, A. García-Sastre, E. R. Stanley, F. Ginhoux, P. S. Frenette, M. Merad, *Immunity* **2013**, *38*, 792.

[49] M. Batten, J. Li, S. Yi, N. M. Kljavin, D. M. Danilenko, S. Lucas, J. Lee, F. J. de Sauvage, N. Ghilardi, *Nat. Immunol.* **2006**, *7*, 929.

[50] J. S. Stumhofer, A. Laurence, E. H. Wilson, E. Huang, C. M. Tato, L. M. Johnson, A. V. Villarino, Q. Huang, A. Yoshimura, D. Sehy, C. J. M. Saris, J. J. O'Shea, L. Hennighausen, M. Ernst, C. A. Hunter, *Nat. Immunol.* **2006**, *7*, 937.

[51] G. Murugaiyan, A. Mittal, R. Lopez-Diego, L. M. Maier, D. E. Anderson, H. L. Weiner, *J. Immunol.* **2009**, *183*, 2435.

[52] L. Zhang, C.-C. Wang, *Hepatobiliary Pancreatic Dis. Int.* **2014**, *13*, 138.